




Article

Oxidation State of the Lithospheric Mantle Beneath Komsomolskaya–Magnitnaya Kimberlite Pipe, Upper Muna Field, Siberian Craton

Anna Dymshits ^{1,2,*} , Igor Sharygin ^{1,2}, Zhe Liu ³, Nester Korolev ^{4,5} , Vladimir Malkovets ^{2,6}, Taisia Alifirova ^{2,7} , Igor Yakovlev ² and Yi-Gang Xu ³

¹ Institute of the Earth's Crust, Siberian Branch of the Russian Academy of Sciences, Irkutsk 664033, Russia; isharygin@igm.nsc.ru

² Sobolev Institute of Geology and Mineralogy, Siberian Branch of Russian Academy of Sciences, Novosibirsk 630090, Russia; vomal@igm.nsc.ru (V.M.); taa@igm.nsc.ru (T.A.); yakistar2020@mail.ru (I.Y.)

³ State Key Laboratory of Isotope Geochemistry, Guangzhou Institute of Geochemistry, Chinese Academy of Sciences, Guangzhou 510640, China; liuzhe@gig.ac.cn (Z.L.); yigangxu@gig.ac.cn (Y.-G.X.)

⁴ Institute of Earth Sciences, Saint-Petersburg State University, St. Petersburg 199034, Russia; nm.korolev@yandex.ru

⁵ Institute of Precambrian Geology and Geochronology, Russian Academy of Sciences, St. Petersburg 199034, Russia

⁶ Geo-Scientific Research Enterprise Public Joint-Stock Company "ALROSA", Republic of Sakha (Yakutia), Mirny 678170, Russia

⁷ Department of Lithospheric Research, University of Vienna, 1090 Vienna, Austria

* Correspondence: adymshits@crust.irk.ru

Received: 13 May 2020; Accepted: 11 August 2020; Published: 21 August 2020



Abstract: The oxidation state of the mantle plays an important role in many chemical and physical processes, including magma genesis, the speciation of volatiles, metasomatism and the evolution of the Earth's atmosphere. We report the first data on the redox state of the subcontinental lithospheric mantle (SCLM) beneath the Komsomolskaya–Magnitnaya kimberlite pipe (KM), Upper Muna field, central Siberian craton. The oxygen fugacity of the KM peridotites ranges from -2.6 to 0.3 logarithmic units relative to the fayalite–magnetite–quartz buffer ($\Delta\log f_{\text{O}_2}$ (FMQ)) at depths of 120–220 km. The enriched KM peridotites are more oxidized (-1.0 – 0.3 $\Delta\log f_{\text{O}_2}$ (FMQ)) than the depleted ones (from -1.4 to -2.6 $\Delta\log f_{\text{O}_2}$ (FMQ)). The oxygen fugacity of some enriched samples may reflect equilibrium with carbonate or carbonate-bearing melts at depths >170 km. A comparison of well-studied coeval Udachnaya and KM peridotites revealed similar redox conditions in the SCLM of the Siberian craton beneath these pipes. Nevertheless, Udachnaya peridotites show wider variations in oxygen fugacity (-4.95 – 0.23 $\Delta\log f_{\text{O}_2}$ (FMQ)). This indicates the presence of more reduced mantle domains in the Udachnaya SCLM. In turn, the established difference in the redox conditions is a good explanation for the lower amounts of resorbed diamonds in the Udachnaya pipe (12%) in comparison with the KM kimberlites (33%). The obtained results advocate a lateral heterogeneity in the oxidation state of the Siberian SCLM.

Keywords: lithospheric mantle; craton; oxidation state; redox state; diamond; xenolith; peridotite; kimberlite; diamond; Siberian craton; mantle metasomatism

1. Introduction

The redox state of the mantle is essential for understanding processes occurring in the Earth's interior. The fugacity of oxygen (f_{O_2}) is a thermodynamic variable that indicates chemical potential

of the oxygen in reactions where both reagents and products contain the same element (s), but with different valence states. In the lithospheric mantle, the oxygen fugacity affects not only the relative abundances of Fe^{3+} and Fe^{2+} in minerals, but also the stability of carbon which can exist in reduced (CH_4 – H_2O fluid, diamond and graphite) or oxidized (CO_2 – H_2O fluid, carbonate melt and carbonates) forms [1–6]. The composition of C–O–H-bearing fluids coexisting with mantle rocks affects their solidus temperature and, hence, the depth of mantle magma generation [4,7,8]. The fugacity of oxygen is a measure of the amount of oxygen available to react with multiple valence elements (e.g., Fe, Cr, V, Ti, Ce, Eu and C) that can be components of mantle minerals of fluids/melts [1–9]. Among these elements, iron is the most abundant in the upper mantle of the Earth and the $\text{Fe}^{3+}/\Sigma\text{Fe}_{(\text{tot})}$ ratio in minerals can be used as an indicator of the redox conditions. In mantle peridotites, garnet may contain significant amounts of Fe^{3+} and, therefore, Fe-rich end-members—skiaegite ($\text{Fe}^{2+}_3\text{Fe}^{3+}_2(\text{SiO}_4)_3$) and andradite ($\text{Ca}_3\text{Fe}^{3+}_2(\text{SiO}_4)_3$)—act as redox sensors in the oxybarometric reactions [10–12].

To date, comprehensive studies of the redox state of the lithospheric mantle underlying the ancient Archean cratons have been carried out on the Kaapvaal (South Africa) and Slave (Canada) cratons [13–17]. These studies have shown that the subcontinental lithospheric mantle (SCLM) is laterally and vertically heterogeneous in terms of its oxidation state (logarithmic units relative to the fayalite–magnetite–quartz buffer; $\Delta\log f\text{O}_2$ (FMQ)). The main processes, governing the observed $f\text{O}_2$ variations in the SCLM are melt extraction from the mantle during SCLM formation and subsequent reactions with mantle fluids or melts (i.e., due to mantle metasomatism) [5,15,18].

Redox conditions for the Siberian cratonic mantle have been constrained based on peridotite xenoliths from the Udachnaya kimberlite pipe only [19–21]. In this paper, we report the first data on the oxygen fugacity ($f\text{O}_2$) of peridotite xenoliths from the diamondiferous Komsomolskaya–Magnitnaya (KM) kimberlite pipe (Upper Muna field). According to Rosen et al. [22], the Udachnaya and KM pipes are coeval, although they are located 150 km apart on different tectonic terrains of the Siberian craton (Figure 1 based on Figure 1 from [23]). Thus, our study provides the first insight into the spatial variations in redox conditions in the SCLM of the Siberian craton in the Upper Devonian–Lower Carboniferous time. We also discuss the $f\text{O}_2$ in the context of different abundances of rounded (i.e., resorbed) diamonds in the KM and Udachnaya pipes.

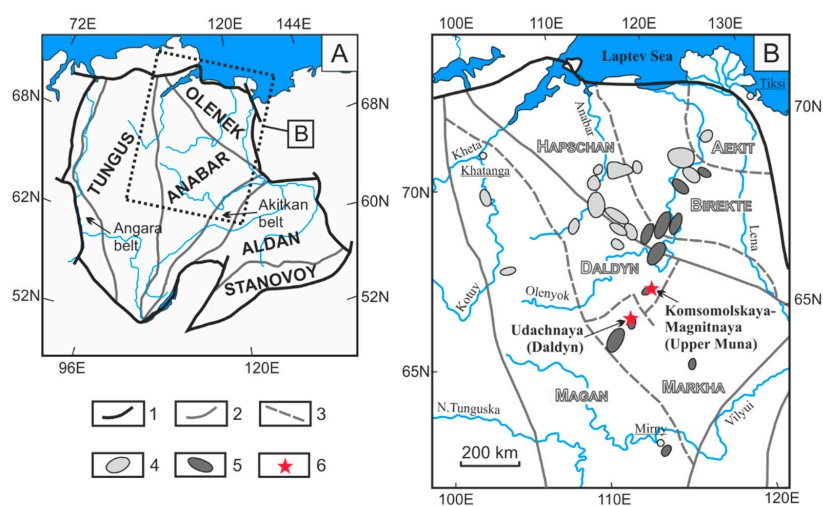


Figure 1. Schematic map (A) of the Siberian craton showing boundaries of the craton (1), its basement structure with boundaries of tectonic provinces (2) and (B) terranes (3) within the provinces and locations of Mesozoic (4) and Paleozoic (5) kimberlite fields (modified after [22]). The kimberlite pipes Udachnaya (Daldyn field, Markha terrane) and Komsomolskaya–Magnitnaya (Upper Muna, Daldyn terrane) described in this study are shown by red stars (6) in panel (B). The Anabar Province consists of the Daldyn, Markha and Magan terranes and the Olenek Province is composed of the Hapschan, Birekte and Aekit terranes.

2. Materials and Methods

2.1. Geological Setting

The Siberian craton is a collage of Archean granulite–gneiss and granite–greenstone blocks and Proterozoic orogenic belts consolidated into a single stable unit at 2.1–1.8 Ga [24–26]. Different terrains of the Siberian craton are grouped into larger units—tectonic provinces: Tungus, Anabar, Olenek, Aldan and Stanovoy (Figure 1). The Anabar province is composed of the three terranes: Daldyn (granulite–gneiss), Markha (granite–greenstone) and Magan (granulite–gneiss) (Figure 1). The faults separating the terranes indicate tectonic compression and are recognized as zones of collision (sutures) [27]. Another key piece of evidence of the collisional boundaries between the terranes is the synchronism of local metamorphism and granitization. U–Pb and Hf-isotope studies of zircons from crustal xenoliths of the Anabar province (Upper Muna, Daldyn, Alakit and Nakyn kimberlite fields) revealed the Archean age (from 3.65 to 3.11 Ga) of the basement rocks. This Paleoproterozoic crust was significantly reworked during several tectonothermal events, including a Neoproterozoic stage (2.9–2.5 Ga) and multiple Paleoproterozoic metamorphisms (1.98, 1.9 and 1.8 Ga) [28–30].

A Yakutian kimberlite province occupies the northeastern part of the Siberian craton and includes five diamondiferous fields: Mirny, Nakyn, Daldyn, Alakit and Upper Muna (Figure 1). Kimberlite magmatism within the Siberian craton is related to four distinct episodes: Silurian–Early Devonian (420–400 Ma), Late Devonian–Early Carboniferous (350–380 Ma), Triassic (215–235 Ma) and Early Cretaceous–Jurassic (140–170 Ma) [31–35]. Diamond-rich kimberlites are overwhelmingly Late Devonian–Early Carboniferous in age. The KM diamondiferous kimberlite is one of the 19 kimberlite bodies in the Upper Muna field. The KM pipe was discovered in the middle of the last century, but mining operations only started in 2019. The pipe consists of two ore bodies (south and west) comprising three types of kimberlite rocks: kimberlite breccia, monticellite-bearing porphyritic kimberlite and monticellite-free porphyritic kimberlite. According to the terminology proposed in [36], kimberlite breccia is defined as kimberlite rocks containing >10 vol% of country rocks, whereas porphyritic kimberlite hosts <10% of country rocks. The KM pipe contains mantle xenoliths, but eclogites are rare [37].

U–Pb macrocrystic zircon or perovskite age data for the KM pipe is not available yet. Recently obtained U–Pb perovskite and macrocrystic zircon ages for six kimberlite pipes from the Upper Muna field showed a narrow range from 367 to 345 Ma [34,38–42], corresponding to the Upper Devonian–Lower Carboniferous time. The emplacement age of the KM pipe is roughly estimated as 334–382 Ma based on the bulk groundmass K–Ar data of kimberlite breccia [43,44]. The Rb–Sr ages of phlogopite megacrysts from the pipe yielded 400–402 Ma [45].

2.2. Samples

The samples were collected in 2012 (TKM ones) and 2018 (AKM ones) from the kimberlites in the small quarries that remained after the bulk sampling of the pipe. Nine xenoliths investigated in this study are within 5–10 cm in the longest dimension and four samples are represented by small (less than 3 cm in diameter) fragments of larger xenoliths. The samples were selected in order to demonstrate a range of metasomatic re-enrichment from dunites and harzburgites to lherzolites.

2.3. Analytical Methods

The major and minor element compositions of the minerals were determined by using a JEOL JXA-8100 microprobe at the Analytical Center for Multi-Elemental and Isotope Research of Siberian Branch of the Russian Academy of Sciences (SB RAS), V.S. Sobolev Institute of Geology and Mineralogy, Novosibirsk, Russia. The analytical conditions were a 20-kV voltage and 100-nA beam current. The counting times were 10 s at the peak and 5 s in the background on each side of the peak for the main elements (Mg, Ti, Ca, Si, Fe, Mn, Ni) and 20 s at the peak and 10 s in the background on each side of the peak for minor elements (Na, Cr, K, Al). Elemental calibration was performed on a range of

well-characterized natural and synthetic in-house standards. The detection limits (3σ) did not exceed (in wt%) 0.01 for CaO and K₂O, 0.02 for Al₂O₃, Cr₂O₃, FeO, MnO, NiO and Na₂O, 0.03 for TiO₂, 0.04 for SiO₂ and 0.14 for MgO.

Trace elements in garnets were measured with an ELEMENT XR (Thermo Fisher Scientific) ICP-SF-MS coupled with a 193-nm (ArF) resonetics RESOLUTION M-50 laser ablation system in the State Key Laboratory of Isotope Geochemistry, Guangzhou Institute of Geochemistry, Chinese Academy of Sciences. The laser conditions were set as follows: repetition rate—6 Hz; energy density—~4 J·cm⁻²; spot size 60 μm in diameter. A smoothing device (The Squid, Laurin Technic) was used to smooth the sample signal. Each spot analysis consisted of a 20-s gas blank collection with the laser off and a 30-s sample signal detection with the laser on. The calibration line for each element was constructed by analyzing the three USGS reference glasses, BCR-2G, BHVO-2G and GSD-1G. The detailed experimental procedure and data reduction strategy are described in Zhang et al. [46]. A USGS reference glass, TB-1G, was measured as an unknown sample. Thirty analyses of TB-1G indicate that most of the elements are within 8% of the reference values, and the analytical precision (2RSD) was better than 10% for most elements.

The valence state of the iron and the Fe³⁺/ΣFe ratio in garnets were determined using an SM-1201 Mössbauer spectrometer at the Institute of Precambrian Geology and Geochronology, Saint-Petersburg, Russia. Measurements were made at room temperature in a constant acceleration mode with a nominal 50 mCi⁵⁷Co source in a Cr matrix. Analyses were applied to the 40–80 mg samples of clean, inclusion- and alteration-free garnet fragments, which were separated from crushed portions of the xenoliths put in ethanol for better observation by hand-picking under a binocular microscope. The spectra were collected with a multichannel analyzer over a velocity range of ±7 mm/s. The velocity was calibrated relative to the metal iron. The spectra were approximated by the sum of Lorentzian form lines using the MOSSFIT[©] (Mössbauer group, Chemical department of the SPbU) software. The relative amounts of Fe²⁺ and Fe³⁺ were determined using the integral intensities of corresponding doublets attributed to ferrous and ferric iron. The probabilities of the Mössbauer effect were assumed to be equal for Fe²⁺ and Fe³⁺ and at different sites. The ratio of Fe³⁺/ΣFe in the minerals was estimated with an error of ±0.005–0.01.

3. Results

3.1. Petrography

The IUGS systematics of igneous rocks [47] are commonly used by researchers for the classification of ultramafic mantle samples. However, these rock types often show substantial alterations in their olivine and pyroxene phases. Although peridotite with a ≤5% clinopyroxene content is classified *sensu stricto* as harzburgite [47], it is often the convention in mantle petrology to refer to rocks with any clinopyroxene as lherzolites and to rocks without evident clinopyroxene as harzburgite. The second described approach is accepted in the present study, in order to be consistent with other works on mantle peridotites. We classified the KM samples according to the nomenclature proposed by Pearson and Brooks [48], i.e., clinopyroxene-free peridotite was defined as harzburgite or dunite (Table 1). Six samples in our collection were classified as harzburgites, six as lherzolites and one as dunite (Figure 2a,b). The dunite xenolith did not contain orthopyroxene.

Table 1. Data derived from the studied peridotites.

Sample No.	AKM 5c	AKM 14	AKM 29l	AKM 36	AKM 45°	AKM 52	AKM 54p	AKM 56	AKM 58	TKM 10/11	TKM 13/11	TKM 26/11	TKM 16/11
Rock type	L	H	H	H	L	D	L	L	H	L	H	H	L
Texture	C	C	C	C	C	C	P	P	C	C	C	C	C
Ol	91	92	90	94	89	97	84	80	93	89	92	92	81
Grt	2	6	4	4	4	3	5	10	3	6	3	3	7
Opx	5	2	6	2	6	–	<1	6	4	1	5	5	2
Cpx	<1	–	–	–	1	–	10	4	–	4	–	–	10
Sp/Phl	–/–	–/–	–/ <1	1/ <1	–/–	–/–	–/–	–/–	–/–	–/–	–/–	–/–	–/–
Garnet class	G9	G10	G10	G10	G9	G10	G9	G9	G9	G9	G10	G10	G9
REE _N pattern	SIN	HUM	HUM	SIN	NOR	SIN	SIN	NOR	NOR	HUM	SIN	SIN	NOR
Fe ³⁺ /ΣFe	0.070	0.104	0.104	0.024	0.104	0.050	0.124	0.140	0.112	0.095	0.055	0.037	0.120
T _{OW79} (°C) P fix	982	974	1010	823	1208	1062	1249	1475	1185	1142	949	979	1158
T _{NG10/T98} (°C)	944	878	958	853	1174	1127	1312	1394	1277	1052	979	989	1118
P _{NG85} (GPa)	4.4	4.3	5.4	3.8	6.0	5.8	6.9	6.7	6.2	5.0	4.5	4.6	5.7
logfO ₂ (ΔFMQ) _{M16}	–1.05	0.26	–1.03	–1.53	–1.98	–2.34	–2.64	–1.95	–1.93	–1.37	–1.40	–2.00	–1.47
logfO ₂ (ΔFMQ) _{S13}	–1.87	–0.91	–1.77	–2.65	–2.44	–2.72	–2.82	–2.22	–2.27	–1.99	–2.17	–2.90	–1.98
T _{OW79} (°C)	995	1146	1037	810	1215	1065	1214	1499	1149	1160	941	975	1216
P _{NG85} (GPa)	4.3	5.1	5.7	3.3	6.5	4.1	5.7	7.8	5.2	5.4	3.7	4.0	6.1
logfO ₂ (ΔFMQ) _{M16}	–1.44	–1.31	–1.48	–1.16	–2.14	–1.85	–2.37	–1.78	–1.39	–2.00	–1.13	–1.91	–1.88
Mg# Grt	82.3	84.5	84.2	84.52	84.4	86.8	82.4	83.6	82.2	85.0	83.7	84.4	83.2
Mg# Ol	92.1	92.4	92.4	93.1	92.6	93.5	91.4	90.6	91.5	91.8	92.7	92.5	92.1

Note: lherzolite (L), harzburgite (H), dunite (d), sinusoidal (SIN), humped (HUM), normal (NOR). Abbreviations for the thermometers and barometers are given in Section 3.4. T_{OW79}—the olivine–garnet thermometer (the estimated error is 60 °C at T < 1300 °C) [49], T_{NG10}—the orthopyroxene–garnet thermometer (the estimated error is 36 °C at T = 900–1200 °C and 25 °C at T > 1200 °C) [50], T_{T98}—the clinopyroxene–orthopyroxene thermometer (the estimated error is 35 °C at T = 900–1200 °C and 25 °C at T > 1200 °C) [51], P_{NG85}—the orthopyroxene–garnet barometer (the estimated error is ±0.3 GPa) [52]. Oxygen fugacity was additionally estimated using the oxybarometers of Miller et al. [12] and Stagno et al. [11], M16 and S13, respectively. olivine (Ol), garnet (Grt), orthopyroxene (Opx), clinopyroxene (Cpx), spinel (Spl) and phlogopite (Phl)—modal abundances in (vol%).

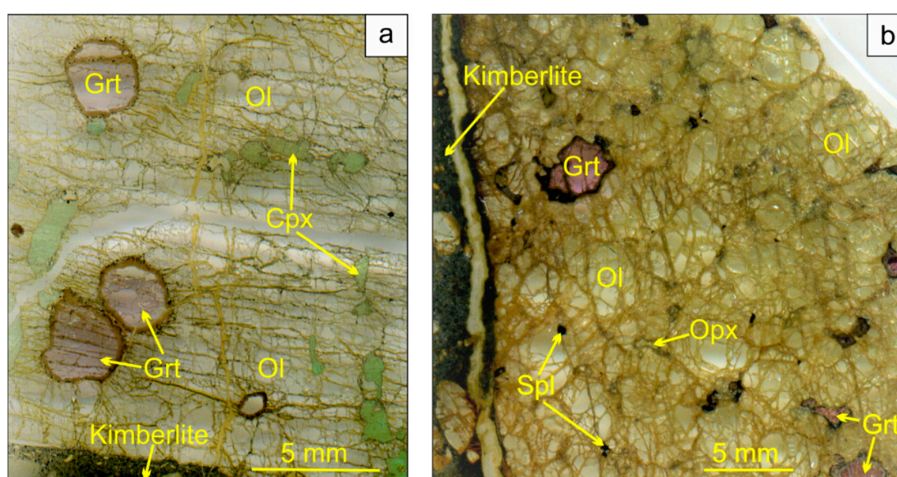


Figure 2. Thin sections of the peridotite xenoliths from the Komsomolskaya–Magnitnaya pipe (visible light scans). (a) Coarse-grained lherzolite xenolith (AKM 45) in contact with the kimberlite; (b) The coarse harzburgite xenolith (AKM 36) in contact with the kimberlite. Symbols: olivine (Ol), garnet (Grt), orthopyroxene (Opx), clinopyroxene (Cpx), spinel (Spl).

The classification proposed by Pearson and Brooks [48] corresponds to the garnet Ca–Cr systematic because the garnet composition in peridotite depends on the presence/absence of clinopyroxene and/or orthopyroxene [53,54]. Garnet from the six samples belongs to the G10 harzburgitic/dunitic group by [54] (Figure 3). The other garnets are plotted within the G9 lherzolite field [54] (Figure 3). However, one (AKM 58) of them neither contains clinopyroxene in the examined thin sections nor in the hand specimen and, thus, should be classified as a harzburgite according to [48].

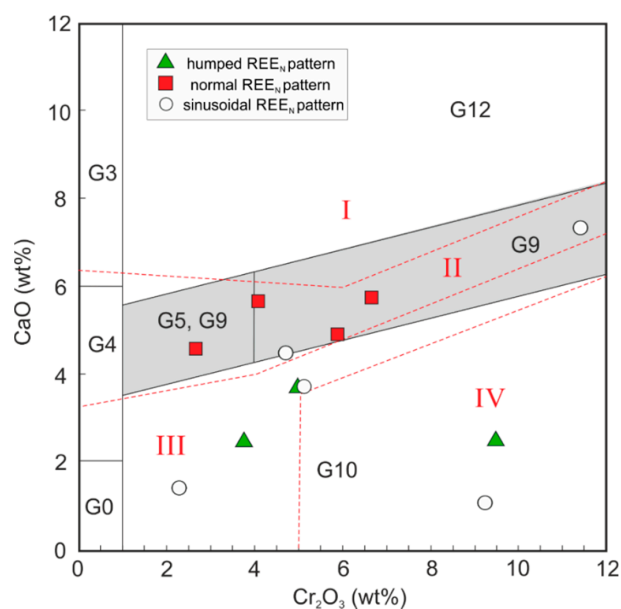


Figure 3. Cr_2O_3 vs. CaO diagram for garnets from the Komsomolskaya–Magnitnaya peridotite xenoliths. G0–G12 fields are after Grütter et al. [54]: G3—eclogitic garnets; G4, G5—pyroxenitic garnets; G9 (overlaps with G5—gray field; the Komsomolskaya–Magnitnaya kimberlite pipe (KM) garnet in the G5 field does not match this field in terms of its TiO_2 content and can be also attributed to the G9)—lherzolitic garnets; G10—harzburgitic garnets; G12—wehrlitic garnets; G0—unclassified category. Fields separated by dashed lines are after Sobolev et al. [53] and denote different mantle parageneses: I—wehrlitic; II—lherzolitic; III—harzburgitic/dunitic; IV—diamondiferous harzburgitic/dunitic.

Eleven samples are coarse and two are porphyroclastic (Table 1, Figure 4a,b), based on the terminology of Harte [55], where textures are defined based on the presence and abundance of olivine porphyroclasts and neoblasts. The coarse peridotites contain granular olivine (up to 1.5 cm), orthopyroxene (0.1–3 mm), rounded garnets (1–5 mm) and irregularly shaped clinopyroxene (Figure 4b). The modal abundance of clinopyroxene in the studied peridotites is usually ≤ 1 vol% (Table 1). However, the TKM 16/11 sample has around 10 vol% of clinopyroxene (Figure 2a). Two coarse samples show that primary-textured equilibrated phlogopite occurred as large tabular grains (AKM 291 and AKM 36) (Figure 4d).

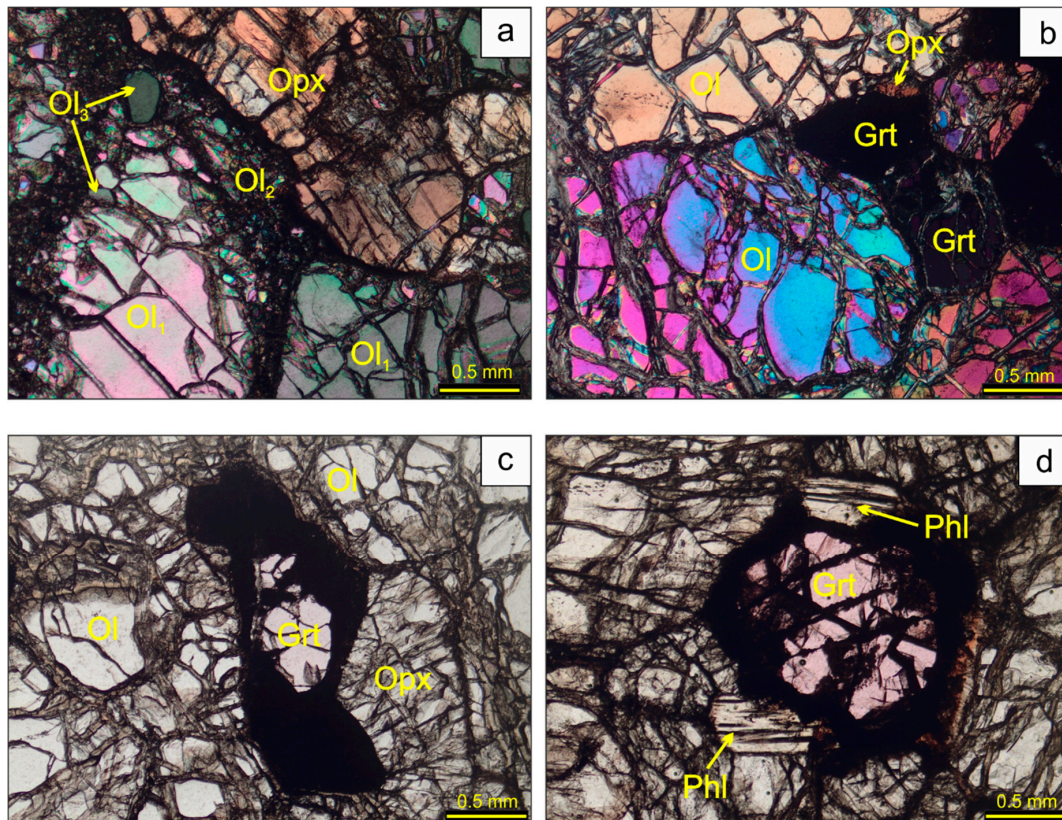


Figure 4. Photomicrographs of mantle xenoliths from the Komsomolskaya–Magnitnaya pipe in (a,b) cross-polarized light and in (c,d) plane-polarized light. Symbols: olivine (Ol), garnet (Grt), orthopyroxene (Opx), clinopyroxene (Cpx), phlogopite (Phl); (a) Iherzolite AKM 54p with porphyroclastic texture. Three types of olivine grains were observed: Ol₁—large porphyroclasts, Ol₂—small neoblasts and Ol₃—euhedral tabular grains; (b) coarse texture of the harzburgite AKM 58 with large olivine crystals (up to 1 cm); (c) harzburgite TKM 26/11 with coarse olivine up to 0.5 cm, orthopyroxene and garnet with black kelyphitic rim; (d) phlogopite grains observed in the coarse-grained harzburgite AKM 291.

Generally, phlogopite is considered to be a product of the modal metasomatism in mantle peridotites [56]. “Primary-textured” or “primary-metasomatic” refers to phlogopite that was formed during mantle metasomatic events that clearly preceded eruption and do not relate to the host magma. Such phlogopite is unzoned and usually represented as large disseminated or clustered grains [57–59]. All studied xenoliths also contain secondary-textured phlogopite as a part of the kelyphitic rims around garnets.

Samples AKM 54p and AKM 56 show porphyroclastic textures, where more than 50% of olivine grains are porphyroclasts. Three types of olivine were found in the AKM 54p peridotite: large porphyroclasts, small polygonal neoblasts and a tabular olivine. The last one is known as a

tablet olivine. The tablet olivine is formed during annealing, postdating the deformation by replacing strained olivine porphyroclasts [60] (Figure 4a). The proportion of olivine neoblasts is higher in AKM 56 than AKM 54p.

All peridotite samples were serpentinized to varying degrees (10–30%).

3.2. Major- and Minor-Element Mineral Composition

Garnets are pyropes with Mg# ($\text{Mg\#(molar)} = 100 \times \text{Mg}/(\text{Mg} + \text{Fe}^{2+})$) ranging from 82.2 to 86.8 (Table 1). Seven garnets are lherzolitic (G9) in composition (Figure 3), with CaO concentrations from 4.42 to 7.32 wt% (Table S1) and Cr_2O_3 content from 2.6 to 11.4 wt%. Another six garnets are identified as harzburgitic/dunitic (G10) with CaO and Cr_2O_3 ranging from 1.42 to 3.74 wt% and from 2.24 to 9.48 wt%, respectively. Two samples fall into the sub-calcic harzburgitic garnet field with $\text{CaO} < 2$ wt%. Total iron, expressed as FeO, in garnets from the KM peridotites, ranges from 6.63 to 7.82 wt%. The garnet $\text{Fe}^{3+}/\Sigma\text{Fe}$ measured using Mössbauer spectroscopy spans from 0.024 to 0.140 (Table 1 and Table S2).

Olivine is forsterite with Mg# ranging from 90.5 to 93.6 (Table S3). Orthopyroxene is identified as enstatite with Mg# = 91.4–93.5, $\text{Cr}_2\text{O}_3 = 0.21$ –0.41 wt%, $\text{Al}_2\text{O}_3 = 0.40$ –0.88 wt% and $\text{Na}_2\text{O} = 0.03$ –0.23 wt% (Table S4). Clinopyroxene is a diopside with Ca# ($\text{Ca\#(molar)} = 100 \times \text{Ca}/(\text{Ca} + \text{Mg} + \text{Fe}) = 34.3$ –43.5, Mg# = 90.5–92.4, $\text{Cr}_2\text{O}_3 = 0.67$ –2.45 wt% and $\text{Al}_2\text{O}_3 = 1.78$ –3.42 wt% (Table S4).

3.3. Trace Element Composition of Minerals

The trace element abundances in the KM garnets are provided in Table S1. Three different chondrite-normalized rare earth element (REE_N) patterns are observed for the xenolith garnets: (1) sinusoidal; (2) humped; and (3) normal (Figure 5) [13,61].

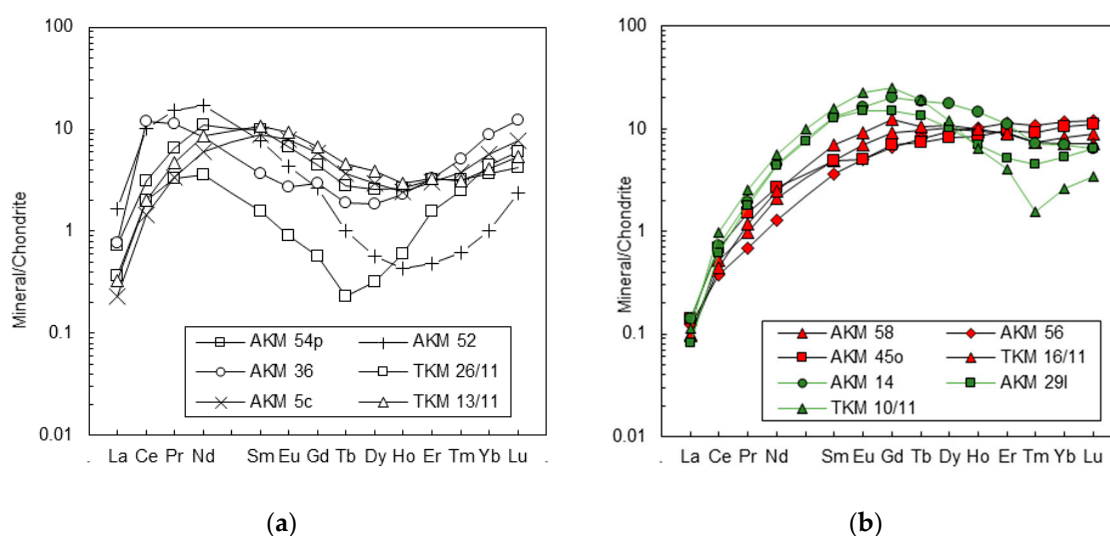


Figure 5. Chondrite-normalized rare earth element (REE_N) patterns of peridotite garnets from the KM xenoliths. CI chondrite values are from [62]. (a) Sinusoidal patterns; (b) normal (red) and humped (green) patterns.

Sinusoidal patterns have two peaks—a positive peak at either Nd (samples AKM 52, TKM 26/11, AKM 54p) or Sm (TKM 13/11, AKM 5c) and a negative one at Er or Tb (TKM 26/11 and AKM 36) (Figure 5a). Humped patterns show a steep positive slope from La to Sm, an almost flat plateau from Sm to Tb at approximately 10–15 chondritic concentrations and a negative MREE to HREE slope (samples AKM 14, 29l and TKM 10/11) (Figure 5b). Garnets with humped REE_N patterns are relatively enriched in Ti, Y and Zr compared to garnets with sinusoidal patterns (Figure 6). Four samples (AKM 14, 45, 56 and 58) have normal REE_N patterns. They look similar to the humped garnets, but with

nearly flat $MREE_N$ – $HREE_N$. These garnets show high Y (up to 20 ppm), Ti (up to 2300 ppm) and moderate Zr (180 ppm) concentrations (Figure 6).

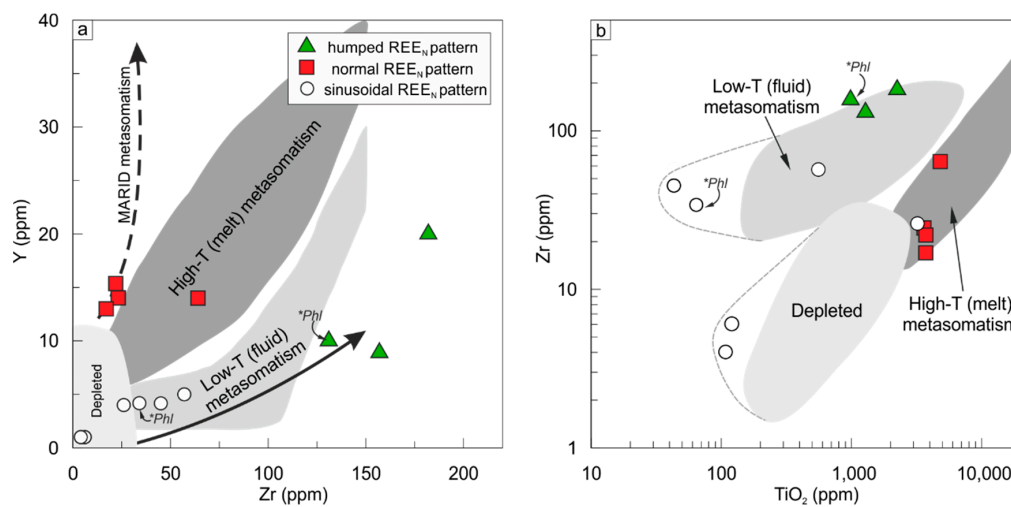


Figure 6. (a) Zr–Y and (b) Zr–TiO₂ patterns of mantle garnets from the KM kimberlite pipe. Fields of depleted garnets; melt-related and fluid-related metasomatism after Griffin and Ryan [63]. White circles represent garnets with sinusoidal REE_N patterns, green triangles—humped and red squares—normal (details provided in the text). Trend for the mica–amphibole–rutile–ilmenite–diopside (MARID) type metasomatism and an arrow for the low-*T* fluid metasomatism in (a) are after [13]. *Samples containing primary-textured phlogopite (Phl).

3.4. Oxythermobarometry

Equilibrated pressures and temperatures were calculated for the mantle xenoliths using conventional tools recommended by Nimis and Grütter [50] for mantle peridotites. We used the orthopyroxene–garnet barometer of Nickel and Green [52] (P_{NG85}), the clinopyroxene–orthopyroxene geothermometer of Taylor [51] (T_{T98}) and the olivine–garnet geothermometer of O’Neill and Wood [49] (T_{ONW79}). Temperatures for clinopyroxene (Cpx)-free samples were obtained with the orthopyroxene–garnet geothermometer proposed by Nimis and Grütter [50] (T_{NG10}). Pressures and temperatures were calculated using the PTQuick software programmed by Dolivo-Dobrovolsky [64].

The geothermometers for mantle-derived garnet peridotites are not internally consistent and may diverge by over 200 °C for the well-equilibrated samples [50]. To assess whether the minerals were in equilibrium, we: (i) studied the core–rim zonation of the samples (only the core compositions were used for P – T calculations); (ii) calculated temperatures using the thermometers mentioned above at pressures obtained from the pair P_{NG85} and T_{T98} (or T_{NG10} for Cpx-free samples). Difference between temperatures (ΔT) calculated for the orthopyroxene (Opx)–garnet (Grt) and Grt–olivine (Ol) pairs should be within the experimental error in case of an equilibrated assemblage of peridotite minerals [14,50]. All studied KM xenoliths show equilibrium between minerals. Differences between calculated temperatures is <95 °C and ten peridotites show $\Delta T < 60$ °C (Table 1).

The samples exhibit a P – T path consistent with the cratonic geotherm with surface heat flux = 35 mW/m², recently obtained for the lithospheric mantle beneath the KM pipe [65] using the FITPLOT program [66] and for the nearby Novinka pipe [67] (Figure 7).

Oxygen fugacity was evaluated relative to the fayalite–magnetite–quartz buffer ($\Delta \log fO_2$ (FMQ)) using the Gt_fO₂ software by Miller et al. [12]. The approach proposed by Miller et al. [12] incorporates four independent oxybarometers and yields optimum $\log fO_2$ estimated by the least squares method. To calculate $\Delta \log fO_2$, we chose to use a combination of P_{NG85} and T_{T98} (or T_{NG10} for the clinopyroxene-free samples) because this pair was recommended as the most robust for mantle peridotites [50]. Oxygen fugacity expressed relative to the fayalite–magnetite–quartz buffer (FMQ) as a

$\Delta \log f_{O_2}$ (FMQ) for KM samples ranging from 0.26 to -2.64 . The uncertainty reported in calculating the f_{O_2} calculated with this method ranges from 0.6–0.9 log units (Figure 8).

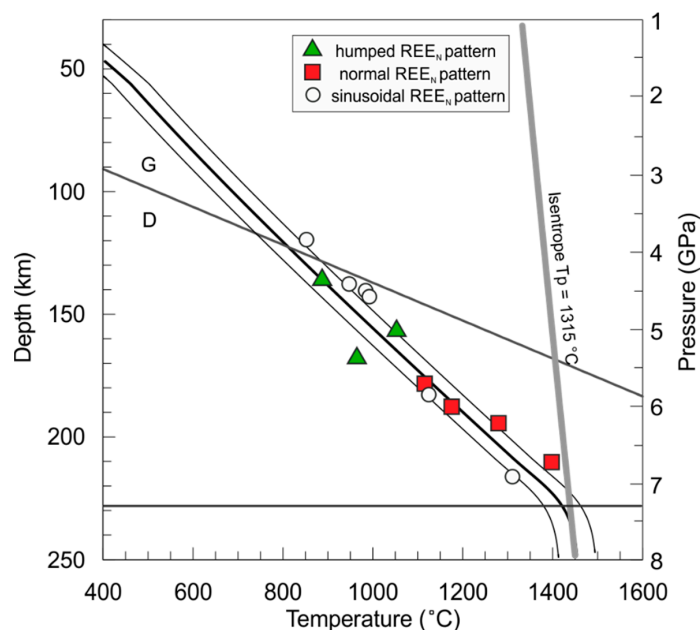


Figure 7. Plot of P_{NG85} against $T_{T98/NG10}$ for the mantle xenolith from the KM pipe. The thick black line represents mantle paleogeotherm beneath the KM pipe [65]. Lines running parallel to the paleogeotherm show the calculated uncertainty. The graphite–diamond transition (G/D) is after [68]. Mantle isentrope with the potential temperature T_p 1315 °C is after [69].

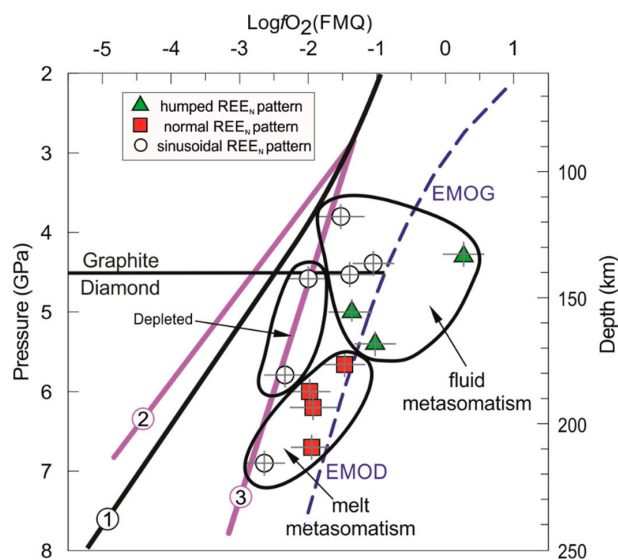


Figure 8. Plots of oxygen fugacity (f_{O_2}) (logarithmic units relative to the fayalite–magnetite–quartz buffer (FMQ) buffer) vs. pressure/depth for garnet peridotite xenoliths from the KM pipe. Fields indicate depleted peridotites and peridotites with the signatures of fluid or melt metasomatic alteration (based on the systematics in Figures 5 and 6). Trend (1) represents the calculated depth– f_{O_2} curve for the pre-metasomatized subcontinental lithospheric mantle (SCLM) [8]. Lines (2) and (3) are f_{O_2} trends for depleted peridotites from the Udachnaya [19] and KM pipes (details are provided in Section 4.2.). The diamond/graphite phase boundary is after [68]. Enstatite–magnesite–olivine–diamond/graphite (EMOD/EMOG) buffer line refers to the reaction of diamond/graphite stability vs. an oxidized form of carbon calculated for the KM mantle paleogeotherm using Equation (14) from Stagno and Frost [70].

Additionally, the $\Delta \log fO_2$ (FMQ) calculated using the combination of T_{ONW79} and P_{NG85} are summarized in Table 1. We have excluded the Fe^{3+} determined by Mössbauer spectroscopy from the total Fe because T_{ONW79} is sensitive to the presence of ferrous iron. We observed that for the low $Fe^{3+}/\Sigma Fe$ values (up to 0.07), temperature increases by up to 60 °C, while for the oxidized samples with the higher $Fe^{3+}/\Sigma Fe$ values, the discrepancy reaches 100–150 °C. Sample AKM 14 has the temperature differences of 270 °C between T_{ONW79} and T_{NG10} . Nimis and Grütter [50], in their extensive review on geothermobarometry, concluded that T_{ONW79} may provide inaccurate estimates, especially for highly oxidized samples (as AKM 14). The $\Delta \log fO_2$ (FMQ) varies within ± 0.1 – 0.6 -log unit for all samples comparing to the $P_{NG85}/T_{NG10}/T_{98}$ pair, excluding AKM 14 due to the strong dependence of fO_2 on the pressure of garnet peridotites (Table 1).

4. Discussion

4.1. Mantle Metasomatism

The Siberian SCLM formed as a residue from a high-degree partial melting of fertile garnet peridotites [71,72]. After the consolidation, the lithosphere of the Siberian craton experienced multiple large-scale metasomatic events [63,73]. Two main types of mantle metasomatism have been described [74–78]: (a) a modal metasomatism, implying the formation of new minerals and (b) a cryptic metasomatism, suggesting changes in the composition of preexisting minerals only [56]. The metasomatic enrichment includes numerous types of metasomatic agents: hydrous and carbonatitic fluids, high-temperature silicate melts, Fe–Ti rich agents and kimberlite fluids [74–76,78–81].

REE_N patterns and trace elements such as Y, Ti and Zr are powerful indicators of metasomatic re-enrichment that occurred in the lithospheric mantle. The most depleted samples from the SCLM are represented by mineral inclusions in diamonds [63]. Griffin and Ryan [63] defined garnets from depleted peridotites as containing low abundances of TiO_2 (<2000 ppm), Zr (<25 ppm) and Y (<12 ppm), whereas metasomatically enriched garnets show higher contents of these elements (Figure 6). The most depleted harzburgitic garnets from diamonds have strongly sinusoidal REE_N patterns, indicating re-enrichment only by the most incompatible elements [61]. Meanwhile almost all SCLM peridotites experienced metasomatic overprint [74,75], except for preserved relicts with the ultra-depleted features [82,83]. Peridotitic garnets with normal and humped REE_N patterns may represent strong metasomatic re-enrichment [13,14].

For the Udachnaya mantle peridotites, Yaxley et al. [19] found that depleted low-Ti garnets have strongly sinusoidal REE_N patterns, whereas enriched high-Ti garnets show normal and weakly sinusoidal REE_N patterns. The enriched samples were equilibrated at pressures of 4.5–6.6 GPa, whereas pressures calculated for the depleted peridotites range wider from 2.6 to 7.1 GPa (Figure 9) [19,38]. This observation indicates that the SCLM beneath the Udachnaya pipe was mainly depleted and then became heterogeneously enriched at the 130–180 km depth range [19,38]. The chemical composition of clinopyroxene and garnet from the Udachnaya sheared peridotites came from the enriched layer, indicating a metasomatic, rather than residual, origin [74,84]. Some of the garnets were affected by silicate metasomatism and became lherzolitic in terms of major elements, but they retained sinusoidal REE_N patterns [74]. These patterns are similar to those of lherzolitic garnets found as inclusions in diamonds [85]. Garnet with normal REE_N patterns could have crystallized from silicate metasomatic melts together with clinopyroxene [74].

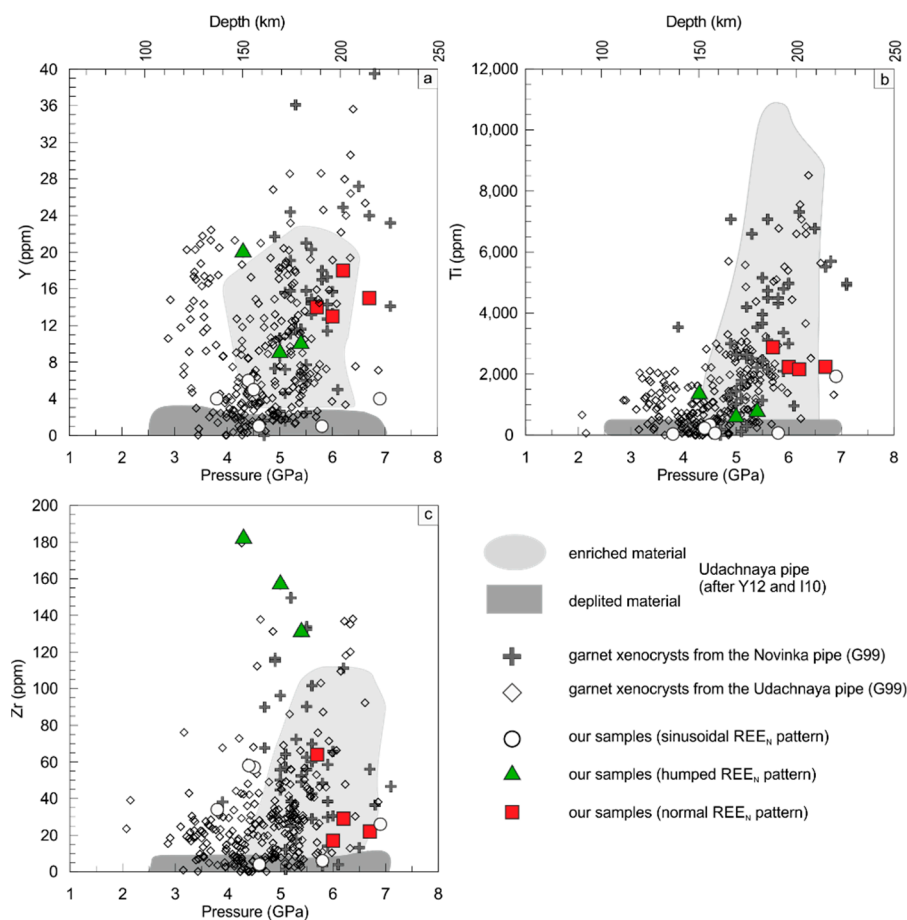


Figure 9. Plot shows (a) Y, (b) Ti and (c) Zr abundance in garnet against equilibration pressures estimated for mantle xenoliths using P_{NG85} . Pressures for garnet xenocrysts [38] were calculated from the equation of mantle paleogeotherm beneath the Novinka pipe [67]. Data for Udachnaya mantle peridotites are after Y12—Yaxley et al. [19] and I10—Ionov et al. [84]. Garnet xenocrysts are from G99 [38]. The subdivision of samples into depleted and enriched is based on the systematics developed in [63].

Two KM garnets (TKM 26/11 and AKM 52) with sinusoidal REE_N patterns show depletion in Ti (<70 ppm), Zr (<10 ppm) and Y (<4 ppm) (Figure 6a). Mineral modes (Cpx-free, low-Opx) and compositions (e.g., high-Cr subcalcic garnets, sinusoidal REE_N patterns) indicate that these xenoliths may represent the depleted residual peridotites with insignificant metasomatic alterations [77]. Another three samples contain garnets with weakly sinusoidal REE_N patterns and a slight enrichment in Zr (up to 58 ppm). These samples are clinopyroxene-free (AKM 5c has less than 1% Cpx) and according to Y–Zr systematics (Figure 6) they were affected by low-temperature fluid metasomatism.

We also studied peridotites that contain garnets with humped REE_N patterns and a high Zr content (130–180 ppm). One of these peridotites (AKM 291) comprises primary-textured phlogopite indicating a low-temperature metasomatism. Notably, although the KM garnets with the humped REE_N patterns contain, in general, more Zr (130–180 ppm) than garnets from the Udachnaya peridotites (<140 ppm) (Figure 9), rare garnet xenocrysts with Zr content > 100 ppm were described from the Udachnaya kimberlites [38].

Phlogopite may be related to different types of metasomatic agents. Some researchers [86,87] provided data on the crystallization of phlogopite together with clinopyroxene in the lithospheric mantle in the presence of kimberlite-related melts: garnet + orthopyroxene + melt = phlogopite + diopside [88,89]. The KM harzburgite xenoliths (AKM 36 and AKM 291 with G10 garnets) contain primary-textured phlogopite, but no clinopyroxene. This may indicate that the KM harzburgites were

metasomatized by a hydrous fluid enriched in mobile potassium and depleted in calcium rather than a kimberlite-related melt. The low-temperature phlogopite metasomatism is accompanied by increasing Zr content. Three out of thirteen KM peridotites have garnets with a Zr content much higher than that reported for garnets from the Udachnaya peridotites (Figure 9) [19,84]. Thus, the SCLM beneath the KM pipe at 130–170 km depth was reworked by the low-temperature phlogopite metasomatism more significantly than the SCLM beneath the Udachnaya pipe.

The KM garnets with normal REE_N patterns are enriched in Ti (>2200 ppm), Zr (>20 ppm) and Y (>13 ppm). Four samples with such garnets also contain a lot of clinopyroxene (up to 10 vol%) and may indicate interaction with the silicate melt or the MARID type of metasomatism as suggested by garnet Y–Zr systematics [63]. On the one hand, Creighton et al. [13] described garnets with Y enrichment and low Zr content and interpreted such geochemical signatures as fingerprints of a melt/fluid metasomatism similar to the mica–amphibole–rutile–ilmenite–diopside (MARID) type. However, silicate modal and cryptic metasomatisms initiated by asthenospheric melts with a composition resembling a mix of ocean island basalts (OIB) and kimberlites have been established in mantle peridotites from the Udachnaya pipe [74].

Ionov et al. [78] showed that the base of the Siberian lithosphere was affected by different metasomatic agents. The sheared Siberian peridotites were subdivided into two groups based on the modal amount of rock-forming minerals (clinopyroxene and garnet), their compositions and garnet REE_N patterns [78]. The first group of peridotites contain high amount of clinopyroxene and garnets with normal REE_N patterns; thus, they were strongly affected by metasomatic agents. The second group is presented by Cpx-poor peridotites with garnets that have a sinusoidal REE_N pattern; thus, such peridotites were slightly metasomatized comparing to the first group. Some KM xenoliths were also identified as sheared peridotites. They have different modal abundances of clinopyroxene and garnet. The AKM56 sheared peridotite contains >6 vol% clinopyroxenes and >10 vol% garnets with normal REE_N patterns. The AKM54p is a sheared Cpx-poor peridotite containing garnet with sinusoidal REE_N patterns. Thus, metasomatic interaction at the base of the lithospheric mantle beneath the KM pipe may have a localized nature and a different degree similar to the SCLM beneath the Udachnaya pipe [78]. Agashev et al. [74] defined three different types of metasomatic enrichment related to the Udachnaya sheared peridotite xenoliths: hydrous or carbonatitic fluid, silicate and an Fe-rich metasomatic. Additional studies are required to describe the composition of the metasomatic melts/fluids at the base of the SCLM beneath the KM pipe.

The KM xenoliths are represented only as peridotites derived from the depth range of 120–230 km (4–7 GPa) and do not cover the entire SCLM column beneath the KM pipe. We described the extensively developed fluid (phlogopite) metasomatism at 130–170 km depth caused by hydrous fluid enriched in K and depleted in Ca. The melt metasomatism beneath the KM pipe was revealed at a 170–220 km depth. Griffin et al. [38] reported geochemical data for the peridotite-derived garnet xenocrysts from the Novinka pipe. The Novinka and KM pipes are situated in 50 m apart and may have a single feeder dike [36] and, thus, could sample the same mantle column. The provided data confirm that the SCLM beneath the Upper Muna field was predominantly affected by a melt metasomatism at depths of 170 km and deeper, whereas the fluid metasomatism was prevalent at shallower depths (Figure 10a). The distribution of fluid and melt-metasomatized garnet peridotites in the SCLM beneath the Udachnaya pipe is more complex [38]. Several peaks indicating different metasomatic events at a wide range of depths (100–210 km) have been revealed (Figure 10b).

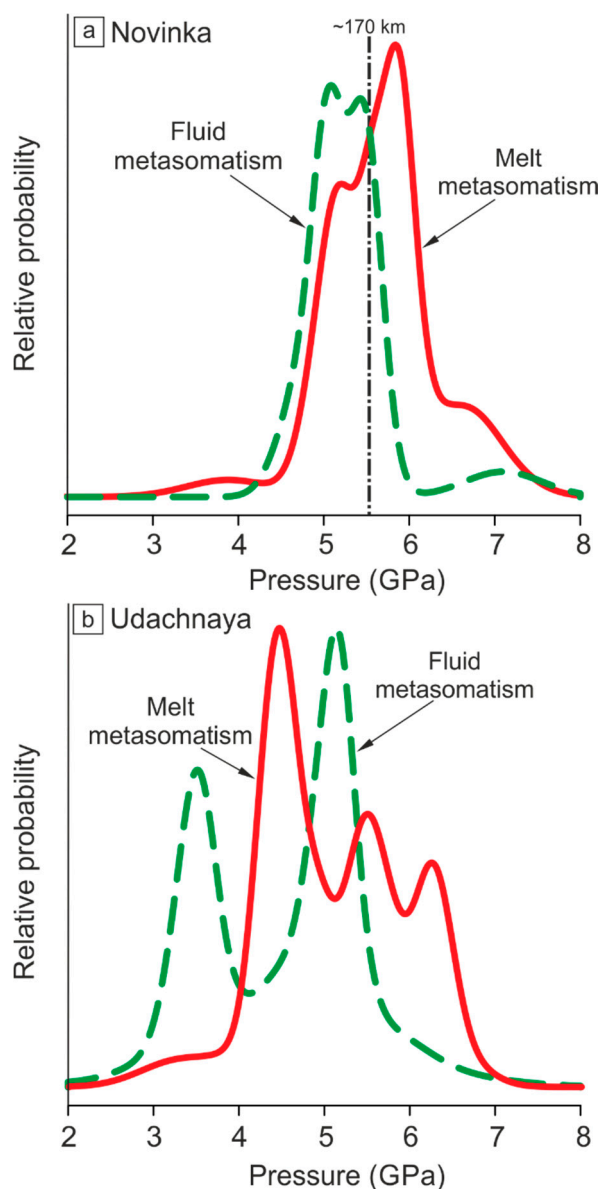


Figure 10. Pressure distribution of melt and fluid metasomatized (based on Zr–Y classification proposed in [63]) garnet xenocrysts [38] from the (a) Novinka and (b) Udachnaya pipes. Pressures were calculated using temperatures proposed for the xenocryst in combination with the mantle paleogeotherms for the Novinka [67] and Udachnaya [65] pipes.

4.2. Oxidation State of SCLM Beneath the KM Pipe

Experimental studies propose the relatively incompatible behavior of Fe^{3+} in comparison with Fe^{2+} during the partial melting of peridotitic mantle [5,90,91]. High degrees of partial melting (20–40%), typical for cratonic peridotites, lead to a progressive decrease in $f\text{O}_2$ for solid residue (e.g., [17,90,91]). Metasomatisms can both oxidize and reduce mantle minerals, depending on the type of metasomatic agent (e.g., CO_2 -rich melt vs. CH_4 fluid) [7,8,92]. However, mantle peridotites showing modal and cryptic metasomatic signatures, in general, have higher $f\text{O}_2$ values in contrast to depleted peridotites [13,19]. Thus, the lowest $f\text{O}_2$ of pre-metasomatized SCLM can be potentially estimated from xenoliths of depleted peridotites, which show evidence of a slight metasomatic alteration. Frost and McCammon [8] calculated the depth– $f\text{O}_2$ curve for the garnet peridotite (trend #1 in Figure 11a), which is usually used as a reference trend for the pre-metasomatic SCLM [13,21].

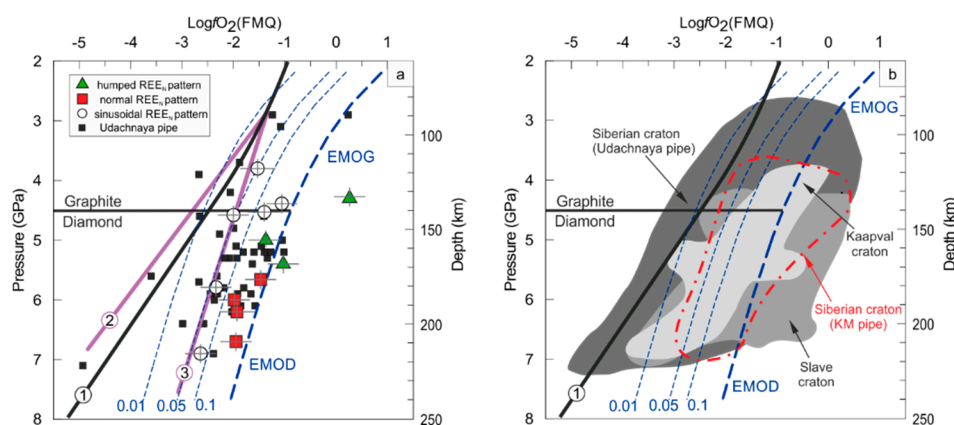


Figure 11. (a) $\Delta\log f_{O_2}$ (FMQ)_{M16} vs. pressure diagram for garnet peridotite xenoliths from the KM and Udachnaya (solid black squares) pipes. Oxygen fugacity for the Udachnaya pipe (black squares) was recalculated by means of the oxybarometer from [12] using original data from [19,21]; (b) variations in the oxygen fugacity calculated for different localities after Miller et al. [12]. Trends (1), (2), (3), diamond/graphite and EMOD/EMOG transitions are similar to Figure 8. Blue thin dashed lines (calculated Equation (14) from [70]) represent oxygen fugacity for carbonate-bearing melt (CO_2 mole fraction is indicated by values 0.01, 0.05 and 0.1) coexisting with diamond/graphite.

Yaxley et al. [19] showed that depleted garnet peridotites from the Udachnaya pipe form an approximately linear trend where f_{O_2} decreases with depth. This trend is almost identical to curve of the “pre-metasomatic” SCLM from [8] (trend #2 Figure 11). This means that the depleted samples from the Udachnaya pipe underwent only minor metasomatic oxidation and reenrichment. Enriched garnet peridotites from the Udachnaya pipe show $\Delta\log f_{O_2}$ (FMQ) of 1–2 units higher than the depleted samples. This difference indicates a clear link between metasomatism and oxidation [19] (Figure 11). Oxygen fugacity estimates for the Udachnaya peridotites obtained by Goncharov et al. [21] are consistent with the data published by Yaxley et al. [19].

The KM-depleted peridotites (trend #3 in Figure 11a) are generally more oxidized than the depleted peridotites from the Udachnaya pipe (trend #2 in Figure 11a) [19] at depths of 120–220 km. Moreover, KM harzburgites/dunites, representing the most depleted peridotites, are more oxidized than some Udachnaya enriched lherzolites. The comparison point out that the SCLM beneath the Daldyn field (Udachnaya pipe) consists of more heterogeneous material (-4.95 – 0.23 $\Delta\log f_{O_2}$ (FMQ)) than the SCLM beneath the Upper Muna field (KM pipe) (-2.6 – 0.3 $\Delta\log f_{O_2}$ (FMQ)). Although the $\Delta\log f_{O_2}$ (FMQ) estimations for the KM and Udachnaya peridotites overlap, it cannot be denied that some peridotites from the Udachnaya pipe are more reduced (the difference can reach up to 2.5 $\Delta\log f_{O_2}$ (FMQ)). This may indicate reduced domains of depleted peridotites in the SCLM beneath the Udachnaya pipe.

The reduced depleted samples from the Udachnaya pipe give evidence of the absence of carbonate or carbonated silicate melts at the depths of 170–220 km, but they are also in agreement with the reduced $CH_4 + H_2O$ asthenospheric fluids [19,21,93] or reduced silicate melts [94]. The KM samples are too oxidized to be in equilibrium with highly reduced fluids. The depleted peridotites, from a depth of 170–220 km, overlap with the stability field of the melt, which can contain up to 0.05 moles of CO_2 (Figure 11).

Different types of metasomatic agents (low- T fluid and melt/MARID) could affect the f_{O_2} , as suggested by the REE_N patterns in garnets, and the Y–Zr–TiO₂ systematics. Fluid-metasomatized samples from the KM pipe do not show an apparent depth– f_{O_2} trend, but, instead, span the range from -1.5 to 0.3 $\Delta\log f_{O_2}$ (FMQ) between 135 and 165 km (Figure 11a). All samples, including those with sinusoidal REE_N patterns in garnets, are more oxidized than the oxidation predicted by trend #1 (Figure 11a). This suggests that fluid-metasomatized agents may cause extensive oxidation of the lithospheric mantle. The most oxidized KM samples cross the

enstatite–magnesite–olivine–diamond/graphite (EMOG/D) reaction boundary [70] (Figure 11) and, therefore, the carbon in these peridotites is able to exist in the form of carbonate phases.

The melt-metasomatized samples show a decrease in the $\Delta\log f_{\text{O}_2}$ (FMQ) from -1.5 at ~ 170 km to -2.6 at ~ 220 km (Figure 11b). The trend formed by these samples is close to the enstatite–magnesite–olivine–diamond/graphite (EMOD/EMOG) buffer [70]. Peridotites containing garnets with normal REE_N patterns may intersect the buffer, taking the uncertainties into account. The presence of a carbonate-bearing oxidized melt (e.g., carbonate or carbonated silicate) shifts the diamond/graphite–carbonate equilibrium towards the lower f_{O_2} and constricts the stability field of diamond/graphite [6,70,95,96]. All studied KM samples are beyond the diamond stability field if the melt contains 0.05 moles of CO_2 (Figure 11). Thus, the interaction of the carbonatitic and/or carbonated silicate melt with the peridotitic mantle beneath the KM pipe could produce a destructive environment for diamonds.

In contrast to the Daldyn field, diamond deposits in the Upper Muna field are characterized by a higher content of rounded diamonds. For instance, the KM and Novinka pipes have 33% and 17% of rounded diamonds, respectively, vs. 12% of rounded diamonds in the Udachnaya pipe [97,98]. The rounded shape of diamonds is interpreted as a result of a dissolution into melts/fluids [99–101]. The dissolution of diamonds may occur in kimberlite magma during their transportation from the mantle to the Earth's surface or in situ in the mantle due to the metasomatic reaction of diamond-bearing rocks with oxidizing melt/fluid [101–106]. The SCLM beneath the Udachnaya pipe is more heterogeneous in terms of f_{O_2} than the SCLM beneath the KM pipe (Figure 11). The amount of depleted material, expressed as a percentage of depleted garnet xenocrysts (based on the data from [38]) beneath the Udachnaya pipe (23%) is much higher than beneath the pipes within the Upper Muna field (5%). A combination of these facts may explain the lower amounts of resorbed diamonds in the Udachnaya pipe in comparison with the KM and Novinka kimberlites. It is interesting to note that the Mir and Internationalnaya pipes (Mirny field, Magan terrane) are characterized by the absence of rounded diamonds [36,107,108]. This motivates us to continue our research on the oxidation state of the Siberian SCLM.

A review of the redox state of the SCLM beneath different regions was published in a recent study by Rielli et al. [109] who reported that the oxygen fugacity of kimberlite xenoliths ranges from -4.9 to $+1.5$ $\Delta\log f_{\text{O}_2}$ (FMQ). However, Rielli et al. [109] did not indicate particular cratons. Goncharov et al. [21] compared the SCLM of the Siberian, Slave and Kaapvaal cratons and showed that the first two are more oxidized. We observe that, at a similar depth, the f_{O_2} for garnet peridotites from KM varies over a broader range, both with more reduced and more oxidized values than those from the Kaapvaal craton [13,16,93,110] (Figure 11b). The $\Delta\log f_{\text{O}_2}$ (FMQ) of the Slave peridotites varies from -4.11 to $+0.95$ log units using the oxybarometer by Stagno et al. [11] and from -3.85 to $+0.44$ log units using Miller et al. [12] over a P – T range from 2.0 to 8.4 GPa [12,14,15]. Thus, the redox conditions of the SCLM beneath the KM pipe, Kaapvaal and Slave cratons are comparable (Figure 11b). In general, the Siberian craton is more heterogeneous and shows wider variations in f_{O_2} (Figure 11b).

5. Conclusions

- The first Mössbauer-based oxygen fugacity estimations for 13 peridotite xenoliths from the KM pipe (Upper Muna field) showed a relatively narrow range, from -2.6 to 0.3 $\Delta\log f_{\text{O}_2}$ (FMQ) at depths of 120–220 km;
- The SCLM beneath the Upper Muna field was affected by a melt metasomatism at depths of 170 km and deeper, whereas a fluid metasomatism was prevalent at shallower depths. In the Udachnaya pipe (Daldyn field), fluid- and melt-metasomatized garnet xenoliths had a more complex distribution in the lithospheric column;
- Garnets from three out of thirteen studied KM peridotite xenoliths show a much higher Zr content (up to 180 ppm) than garnets from the Udachnaya peridotites (135 ppm). This indicates that

the SCLM beneath the KM pipe at a 130–170-km depth was reworked by a low-temperature phlogopite metasomatism more significantly than the SCLM beneath the Udachnaya pipe;

- The redox conditions recorded by the studied KM peridotites (-2.6 to $0.3 \Delta \log fO_2$ (FMQ)) are comparable to the redox state of the SCLM beneath the Udachnaya pipe (-4.95 to $0.23 \Delta \log fO_2$ (FMQ)). However, the SCLM beneath the Udachnaya pipe may comprise more reduced mantle domains. Thus, the established difference between the KM and Udachnaya peridotites may indicate a lateral heterogeneity in the oxidation conditions of the Siberian SCLM.

Supplementary Materials: The following are available online at <http://www.mdpi.com/2075-163X/10/9/740/s1>, Table S1: Garnet compositions from the Komsomolskaya–Magnitnaya garnet peridotites. Table S4: Mössbauer hyperfine parameters (QS—quadrupole splitting, IS—isomer shift in mm/s, HW—half width of peak in mm/s) and Fe²⁺ and Fe³⁺ percentages for the Komsomolskaya–Magnitnaya peridotite garnets. Table S3: Olivine compositions from the Komsomolskaya–Magnitnaya garnet peridotites. Table S4: Pyroxenes compositions from the Komsomolskaya–Magnitnaya garnet peridotites.

Author Contributions: Conceptualization, A.D. and I.S.; data curation, A.D. and N.K.; formal analysis, A.D., Z.L., N.K. and I.Y.; funding acquisition, A.D., V.M. and Y.-G.X.; methodology, A.D. and I.S.; resources, V.M., I.Y. and T.A.; software, A.D., Z.L. and N.K.; supervision, I.S. and Y.-G.X.; validation, I.S.; visualization, A.D.; writing—original draft, A.D. and I.S.; writing—review & editing, Z.L., N.K., V.M. and T.A. All authors have read and agreed to the published version of the manuscript.

Funding: The study was supported by the Russian Science Foundation, grant No. 18-77-00070 (sampling, sample preparation). Electron microprobe analyses were funded by the Russian Science Foundation, grant No 18-17-00249.

Acknowledgments: We would like to thank A. Goncharov for the assistance with the Mössbauer measurements, D. Mikhailenko and Le Zhang for the support in with ICP MS measurements, Prof. Bill Griffin for providing original data for the Udachnaya and Novinka garnet xenocrysts and E. Kovaleva for extensive English editing.

Conflicts of Interest: The authors declare no conflict of interest.

References

1. Kadik, A.A.; Sobolev, N.V.; Zharkova, E.V.; Pokhilenko, N.P. Redox conditions of formations of diamond-bearing peridotite xenoliths from Udachnaya kimberlite pipe, Yakutia. *Geokhimiya* **1989**, *27*, 1120–1135.
2. Eggler, D.H. The effect of CO₂ upon partial melting of peridotite in the system Na₂O-CaO-Al₂O₃-MgO-SiO₂-CO₂ to 35 kb, with an analysis of melting in a peridotite-H₂O-CO₂ system. *Am. J. Sci.* **1978**, *278*, 305–343. [[CrossRef](#)]
3. Foley, S.F.; Yaxley, G.M.; Rosenthal, A.; Buhre, S.; Kiseeva, E.S.; Rapp, R.P.; Jacob, D.E. The composition of near-solidus melts of peridotite in the presence of CO₂ and H₂O between 40 and 60 kbar. *Lithos* **2009**, *112*, 274–283. [[CrossRef](#)]
4. Taylor, W.R.; Green, D.H. Measurement of reduced peridotite-C-O-H solidus and implications for redox melting of the mantle. *Nature* **1988**, *332*, 349–352. [[CrossRef](#)]
5. Wood, B.J.; Bryndzia, L.T.; Johnson, K.E. Mantle oxidation state and its relationship to tectonic environment and fluid speciation. *Science* **1990**, *248*, 337–345. [[CrossRef](#)]
6. Stagno, V. Carbon, carbides, carbonates and carbonatitic melts in the Earth's interior. *J. Geol. Soc.* **2019**, *176*, 375–387. [[CrossRef](#)]
7. Foley, S.F. A reappraisal of redox melting in the Earth's mantle as a function of tectonic setting and time. *J. Pet.* **2011**, *52*, 1363–1391. [[CrossRef](#)]
8. Frost, D.J.; McCammon, C.A. The redox state of Earth's mantle. *Annu. Rev. Earth Planet. Sci.* **2008**, *36*, 389–420. [[CrossRef](#)]
9. Ballhaus, C.; Berry, R.F.; Green, D.H. High pressure experimental calibration of the olivine-orthopyroxene-spinel oxygen geobarometer: Implications for the oxidation state of the upper mantle. *Contrib. Miner. Pet.* **1991**, *107*, 27–40. [[CrossRef](#)]
10. Gudmundsson, G.; Wood, B.J. Experimental tests of garnet peridotite oxygen barometry. *Contrib. Miner. Pet.* **1995**, *119*, 56–67. [[CrossRef](#)]
11. Stagno, V.; Ojwang, D.O.; McCammon, C.A.; Frost, D.J. The oxidation state of the mantle and the extraction of carbon from Earth's interior. *Nature* **2013**, *493*, 84–88. [[CrossRef](#)] [[PubMed](#)]

12. Miller, W.G.R.; Holland, T.J.B.; Gibson, S.A. Garnet and spinel oxybarometers: New internally consistent multi-equilibria models with applications to the oxidation state of the lithospheric mantle. *J. Pet.* **2016**, *57*, 1199–1222. [[CrossRef](#)]
13. Creighton, S.; Stachel, T.; Matveev, S.; Hofer, H.; McCammon, C.; Luth, R.W. Oxidation of the Kaapvaal lithospheric mantle driven by metasomatism. *Contrib. Miner. Pet.* **2009**, *157*, 491–504. [[CrossRef](#)]
14. Creighton, S.; Stachel, T.; Eichenberg, D.; Luth, R.W. Oxidation state of the lithospheric mantle beneath diavik diamond mine, central slave craton, NWT, Canada. *Contrib. Miner. Pet.* **2010**, *159*, 645–657. [[CrossRef](#)]
15. Yaxley, G.; Berry, A.; Rosenthal, A.; Woodland, A.; Paterson, D. Redox preconditioning deep cratonic lithosphere for kimberlite genesis—evidence from the central slave craton. *Sci. Rep.* **2017**, *7*, 30. [[CrossRef](#)]
16. Lazarov, M.; Woodland, A.B.; Brey, G.P. Thermal state and redox conditions of the Kaapvaal mantle: A study of xenoliths from the Finsch mine, South Africa. *Lithos* **2009**, *112*, 913–923. [[CrossRef](#)]
17. McCammon, C.; Kopylova, M.G. A redox profile of the slave mantle and oxygen fugacity control in the cratonic mantle. *Contrib. Miner. Pet.* **2004**, *148*, 55–68. [[CrossRef](#)]
18. Woodland, A.B.; Kornprobst, J.; Tabit, A. Ferric iron in orogenic lherzolite massifs and controls of oxygen fugacity in the upper mantle. *Lithos* **2006**, *89*, 222–241. [[CrossRef](#)]
19. Yaxley, G.M.; Berry, A.J.; Kamenetsky, V.S.; Woodland, A.B.; Golovin, A.V. An oxygen fugacity profile through the Siberian craton—Fe K-edge XANES determinations of Fe³⁺/Fe in garnets in peridotite xenoliths from the Udachnaya East kimberlite. *Lithos* **2012**, *140*, 142–151. [[CrossRef](#)]
20. Pokhilenko, L.N.; Pokhilenko, N.P.; Fedorov, I.I.; Tomilenko, A.A.; Usova, L.V.; Fomina, L.N. Fluid regime peculiarities of the lithosphere mantle of the Siberian platform. In *Deep-seated Magmatism, its Sources and Plumes*; Vladyskin, N.V., Ed.; Russian Academy of Sciences: Irkutsk, Russia, 2008; pp. 122–136.
21. Goncharov, A.G.; Ionov, D.A.; Doucet, L.S.; Pokhilenko, L.N. Thermal state, oxygen fugacity and C-O-H fluid speciation in cratonic lithospheric mantle: New data on peridotite xenoliths from the Udachnaya kimberlite, Siberia. *Earth Planet. Sci. Lett.* **2012**, *357*, 99–110. [[CrossRef](#)]
22. Rosen, O.M.; Manakov, A.V.; Suvorov, V.D. The collisional system in the northeastern Siberian craton and a problem of diamond-bearing lithospheric keel. *Geotectonics* **2005**, *39*, 456–479.
23. Alifirova, T.A.; Pokhilenko, L.N.; Korsakov, A.V. Apatite, SiO₂, rutile and orthopyroxene precipitates in minerals of eclogite xenoliths from Yakutian kimberlites, Russia. *Lithos* **2015**, *226*, 31–49. [[CrossRef](#)]
24. Zonenshain, L.P.; Kuzmin, M.I.; Natapov, L.M. *Geology of the USSR: Plate Tectonic Synthesis*; American Geophysical Union: Washington, DC, USA, 1989; Volume 21.
25. Rosen, O.; Condie, K.C.; Natapov, L.M.; Nozhkin, A. Archean and early proterozoic evolution of the Siberian craton: A preliminary assessment. In *Developments in Precambrian Geology*; Elsevier: Amsterdam, The Netherlands, 1994; Volume 11, pp. 411–459.
26. Smelov, A.P.; Timofeev, V.F. The age of the North Asian Cratonic basement: An overview. *Gondwana Res.* **2007**, *12*, 279–288. [[CrossRef](#)]
27. Rosen, O.M.; Serenko, V.P.; Spetsius, Z.V.; Manakov, A.V.; Zinchuk, N.N. Yakutian kimberlite province: Position in the structure of the Siberian craton and composition of the upper and lower crust. *Geol. I Geofiz.* **2002**, *43*, 3–26.
28. Griffin, W.; Belousova, E.; O'Neill, C.; O'Reilly, S.Y.; Malkovets, V.; Pearson, N.; Spetsius, S.; Wilde, S. The world turns over: Hadean–Archean crust–mantle evolution. *Lithos* **2014**, *189*, 2–15. [[CrossRef](#)]
29. Shatsky, V.S.; Malkovets, V.G.; Belousova, E.A.; Tretiakova, I.G.; Griffin, W.L.; Ragozin, A.L.; Gibsher, A.A.; O'Reilly, S.Y. Tectonothermal evolution of the continental crust beneath the Yakutian diamondiferous province (Siberian craton): U–Pb and Hf isotopic evidence on zircons from crustal xenoliths of kimberlite pipes. *Precambrian Res.* **2016**, *282*, 1–20. [[CrossRef](#)]
30. Shatsky, V.S.; Malkovets, V.G.; Belousova, E.A.; Tretiakova, I.G.; Griffin, W.L.; Ragozin, A.L.; Wang, Q.; Gibsher, A.A.; O'Reilly, S.Y. Multi-stage modification of paleoarchean crust beneath the anabar tectonic province (Siberian craton). *Precambrian Res.* **2018**, *305*, 125–144. [[CrossRef](#)]
31. Agashev, A.M.; Pokhilenko, N.P.; Tolstov, A.V.; Polyanichko, V.V.; Mal'kovets, V.G.; Sobolev, N.V. New age data on kimberlites from the yakutian diamondiferous province. *Dokl. Earth Sci.* **2004**, *399*, 1142–1145.
32. Davies, G.L.; Sobolev, N.V.; Kharkiv, A.D. New data on the age of Yakutian kimberlites (U–Pb zircon method). *Dokl. Akad. Nauk SSSR* **1980**, *254*, 175–179. (In Russian)
33. Kinny, P.D.; Griffin, B.J.; Heaman, L.M.; Brakhfogel, F.F.; Spetsius, Z.V. SHRIMP U–Pb ages of perovskite from Yakutian kimberlites. *Geol. I Geofiz.* **1997**, *38*, 91–99.

34. Sun, J.; Liu, C.-Z.; Tappe, S.; Kostrovitsky, S.I.; Wu, F.-Y.; Yakovlev, D.; Yang, Y.-H.; Yang, J.-H. Repeated kimberlite magmatism beneath Yakutia and its relationship to Siberian flood volcanism: Insights from in situ U–Pb and Sr–Nd perovskite isotope analysis. *Earth Planet. Sci. Lett.* **2014**, *404*, 283–295. [[CrossRef](#)]
35. Tretiakova, I.G.; Belousova, E.A.; Malkovets, V.G.; Griffin, W.L.; Piazzolo, S.; Pearson, N.J.; O'Reilly, S.Y.; Nishido, H. Recurrent magmatic activity on a lithosphere-scale structure: Crystallization and deformation in kimberlitic zircons. *Gondwana Res.* **2017**, *42*, 126–132. [[CrossRef](#)]
36. Kostrovitsky, S.; Spetsius, Z.; Yakovlev, D.; Flaass, G.F.D.; Bogush, I.; Pokhilenko, N. *Atlas of the Igneous Rocks and Diamond Deposits of the Yakut Kimberlite Province*; Pokhilenko, N., Ed.; MPG: Mirniy, Russia, 2015; p. 480.
37. Yakovlev, D.A.; Kostrovitsky, S.I.; Alymova, N.V. Composition features of kimberlites from the upper muna field (Yakutia). *Izv. Earth Sci. Sect. Rans* **2009**, *1*, 111–119. (In Russian)
38. Griffin, W.L.; Ryan, C.G.; Kaminsky, F.V.; O'Reilly, S.Y.; Natapov, L.M.; Win, T.T.; Kinny, P.D.; Ilupin, I.P. The Siberian lithosphere traverse: Mantle terranes and the assembly of the Siberian craton. *Tectonophysics* **1999**, *310*, 1–35. [[CrossRef](#)]
39. Levchenkov, O.A.; Gaidamako, I.M.; Levskii, L.K.; Komarov, A.N.; Yakovleva, S.Z.; Rizvanova, N.G.; Makeev, A.F. U–Pb age of zircon from the Mir and 325 Let Yakutii pipes. *Dokl. Earth Sci.* **2005**, *400*, 99–101.
40. Lepekhina, E.; Rotman, A.; Antonov, A.; Sergeev, S. SIMS SHRIMP U–Pb dating of perovskite from kimberlites of the Siberian platform (Verhнемunskoe and Alakite-Marhinskoe fields). In Proceedings of the 9th International Kimberlite Conference: Extended Abstracts, Frankfurt, Germany, 10–15 August 2008; p. 9IKC-A-00353.
41. Lepekhina, E.; Rotman, A.; Antonov, A.; Sergeev, S. SHRIMP U–Pb zircon ages of Yakutian kimberlite pipes. In Proceedings of the 9th International Kimberlite Conference: Extended Abstracts, Frankfurt, Germany, 10–15 August 2008; p. 9IKC-A-00354.
42. Sun, J.; Tappe, S.; Kostrovitsky, S.I.; Liu, C.-Z.; Skuzovatov, S.Y.; Wu, F.-Y. Mantle sources of kimberlites through time: A U–Pb and Lu–Hf isotope study of zircon megacrysts from the Siberian diamond fields. *Chem. Geol.* **2018**, *479*, 228–240. [[CrossRef](#)]
43. Sarsadskih, N.N.; Blagulkina, V.A.; Silin, Y.I. On the absolute age of the Yakutian kimberlites. *Doklady Akademii Nauk SSR* **1966**, *168*, 420–423. (In Russian)
44. Zaitsev, A.; Smelov, A. *Isotope Geochronology of Rocks of the Yakutian Kimberlite Province*; DPMGI SB RAS: Yakutsk, Russia, 2010. (In Russian)
45. Kostrovitsky, S.I.; Solov'eva, L.V.; Yakovlev, D.A.; Suvorova, L.F.; Sandimirova, G.P.; Travin, A.V.; Yudin, D.S. Kimberlites and megacrystic suite: Isotope-geochemical studies. *Petrology* **2013**, *21*, 127–144. [[CrossRef](#)]
46. Zhang, L.; Ren, Z.-Y.; Xia, X.-P.; Yang, Q.; Hong, L.-B.; Wu, D. In situ determination of trace elements in melt inclusions using laser ablation inductively coupled plasma sector field mass spectrometry. *Rapid Commun. Mass Spectrom.* **2019**, *33*, 361–370. [[CrossRef](#)]
47. Le Bas, M.; Streckeisen, A. The IUGS systematics of igneous rocks. *J. Geol. Soc.* **1991**, *148*, 825–833. [[CrossRef](#)]
48. Pearson, G.; Brooks, N. The formation and evolution of cratonic mantle lithosphere—evidence from mantle xenoliths. In *Treatise on Geochemistry*; Carlson, R.W., Ed.; Elsevier: Amsterdam, The Netherlands, 2014; Volume 3, pp. 255–292.
49. O'Neill, H.S.C.; Wood, B.J. An experimental study of Fe–Mg partitioning between garnet and olivine and its calibration as a geothermometer. *Contrib. Miner. Pet.* **1979**, *70*, 59–70. [[CrossRef](#)]
50. Nimis, P.; Grütter, H. Internally consistent geothermometers for garnet peridotites and pyroxenites. *Contrib. Miner. Pet.* **2010**, *159*, 411–427. [[CrossRef](#)]
51. Taylor, W. An experimental test of some geothermometer and geobarometer formulations for upper mantle peridotites with application to the thermobarometry of fertile lherzolite and garnet websterite. *Neues Jahrb. Für Mineral. Abh.* **1998**, *172*, 381–408.
52. Nickel, K.; Green, D. Empirical geothermobarometry for garnet peridotites and implications for the nature of the lithosphere, kimberlites and diamonds. *Earth Planet. Sci. Lett.* **1985**, *73*, 158–170. [[CrossRef](#)]
53. Sobolev, N.V.; Lavrent'ev, Y.G.; Pokhilenko, N.P.; Usova, L.V. Chrome-rich garnets from the kimberlites of Yakutia and their parageneses. *Contrib. Miner. Pet.* **1973**, *40*, 39–52. [[CrossRef](#)]
54. Grütter, H.S.; Gurney, J.J.; Menzies, A.H.; Winter, F. An updated classification scheme for mantle-derived garnet, for use by diamond explorers. *Lithos* **2004**, *77*, 841–857. [[CrossRef](#)]
55. Harte, B. Rock nomenclature with particular relation to deformation and recrystallisation textures in olivine-bearing xenoliths. *J. Geol.* **1977**, *85*, 279–288. [[CrossRef](#)]

56. Dawson, J.B. Contrasting types of upper mantle metasomatism. In *Kimberlites, II: The Mantle and Crust-Mantle Relationships*; Kornprobst, J., Ed.; Elsevier: Amsterdam, The Netherlands, 1984; pp. 289–294.
57. Yudin, D.S.; Tomilenko, A.A.; Alifirova, T.A.; Travin, A.V.; Murzintsev, N.G.; Pokhilenko, N.P. Results of $^{40}\text{Ar}/^{39}\text{Ar}$ dating of phlogopites from kelyphitic rims around garnet grains (Udachnaya-Vostochnaya kimberlite pipe). *Dokl. Earth Sci.* **2016**, *469*, 728–731. [[CrossRef](#)]
58. Solov'eva, L.V.; Yasnygina, T.A.; Egorov, K.N. Metasomatic parageneses in deep-seated xenoliths from pipes Udachnaya and Komsomol'skaya-Magnitnaya as indicators of fluid transfer through the mantle lithosphere of the Siberian craton. *Russ. Geol. Geophys.* **2012**, *53*, 1304–1323. [[CrossRef](#)]
59. Dawson, J.B. Metasomatism and partial melting in upper-mantle peridotite xenoliths from the lashaine volcano, Northern Tanzania. *J. Pet.* **2002**, *43*, 1749–1777. [[CrossRef](#)]
60. Boullier, A.M.; Nicolas, A. Classification of texture and fabric of peridotite xenoliths from South African kimberlites. *Phys. Chem. Earth* **1975**, *9*, 467–476. [[CrossRef](#)]
61. Stachel, T.; Aulbach, S.; Brey, G.P.; Harris, J.W.; Leost, I.; Tappert, R.; Viljoen, K.S. The trace element composition of silicate inclusions in diamonds: A review. *Lithos* **2004**, *77*, 1–19. [[CrossRef](#)]
62. McDonough, W.F.; Sun, S.S. The composition of the Earth. *Chem. Geol.* **1995**, *120*, 223–253. [[CrossRef](#)]
63. Griffin, W.L.; Ryan, C.G. Trace-elements in indicator minerals-area selection and target evaluation in diamond exploration. *J. Geochem. Explor.* **1995**, *53*, 311–337. [[CrossRef](#)]
64. Dobrovolsky, D.D. PTQuick Software. Available online: <http://www.dimadd.ru/en/Programs/ptquick> (accessed on 1 May 2011).
65. Dymshits, A.M.; Sharygin, I.S.; Malkovets, V.G.; Yakovlev, I.V.; Gibsher, A.A.; Alifirova, T.A.; Vorobei, S.S.; Potapov, S.V.; Garanin, V.K. Thermal state, thickness and composition of the lithospheric mantle beneath the upper muna kimberlite field (Siberian craton) constrained by clinopyroxene xenocrysts and comparison with daldyn and mirny fields. *Minerals* **2020**, *10*, 549. [[CrossRef](#)]
66. Mather, K.A.; Pearson, D.G.; McKenzie, D.; Kjarsgaard, B.A.; Priestley, K. Constraints on the depth and thermal history of cratonic lithosphere from peridotite xenoliths, xenocrysts and seismology. *Lithos* **2011**, *125*, 729–742. [[CrossRef](#)]
67. Ziberna, L.; Nimis, P.; Kuzmin, D.; Malkovets, V.G. Error sources in single-clinopyroxene thermobarometry and a mantle geotherm for the Novinka kimberlite, Yakutia. *Am. Miner.* **2016**, *101*, 2222–2232. [[CrossRef](#)]
68. Kennedy, C.S.; Kennedy, G.C. The equilibrium boundary between graphite and diamond. *J. Geophys. Res.* **1976**, *81*, 2467–2470. [[CrossRef](#)]
69. McKenzie, D.; Bickle, M.J. The volume and composition of melt generated by extension of the lithosphere. *J. Pet.* **1988**, *29*, 625–679. [[CrossRef](#)]
70. Stagno, V.; Frost, D.J. Carbon speciation in the asthenosphere: Experimental measurements of the redox conditions at which carbonate-bearing melts coexist with graphite or diamond in peridotite assemblages. *Earth Planet. Sci. Lett.* **2010**, *300*, 72–84. [[CrossRef](#)]
71. Ionov, D.A.; Doucet, L.S.; Carlson, R.W.; Golovin, A.V.; Korsakov, A.V. Post-Archean formation of the lithospheric mantle in the central Siberian craton: Re–Os and PGE study of peridotite xenoliths from the Udachnaya kimberlite. *Geochim. Cosmochim. Acta* **2015**, *165*, 466–483. [[CrossRef](#)]
72. Doucet, L.S.; Ionov, D.A.; Golovin, A.V.; Pokhilenko, N.P. Depth, degrees and tectonic settings of mantle melting during craton formation: Inferences from major and trace element compositions of spinel harzburgite xenoliths from the Udachnaya kimberlite, central Siberia. *Earth Planet. Sci. Lett.* **2012**, *359–360*, 206–218. [[CrossRef](#)]
73. Shu, Q.; Brey, G.P. Ancient mantle metasomatism recorded in subcalcic garnet xenocrysts: Temporal links between mantle metasomatism, diamond growth and crustal tectonism. *Earth Planet. Sci. Lett.* **2015**, *418*, 27–39. [[CrossRef](#)]
74. Agashev, A.M.; Ionov, D.A.; Pokhilenko, N.P.; Golovin, A.V.; Cherepanova, Y.; Sharygin, I.S. Metasomatism in lithospheric mantle roots: Constraints from whole-rock and mineral chemical composition of deformed peridotite xenoliths from kimberlite pipe Udachnaya. *Lithos* **2013**, *160*, 201–215. [[CrossRef](#)]
75. Howarth, G.H.; Barry, P.H.; Fisher, J.F.P.; Baziotis, I.P.; Pokhilenko, N.P.; Pokhilenko, L.N.; Bodnar, R.J.; Taylor, L.A.; Agashev, A.M. Superplume metasomatism: Evidence from Siberian mantle xenoliths. *Lithos* **2014**, *184*, 209–224. [[CrossRef](#)]
76. Shimizu, N.; Pokhilenko, N.P.; Boyd, F.R.; Pearson, D.G. Geochemical characteristics of mantle xenoliths from Udachnaya kimberlite pipe. *Geol. I Geofiz.* **1997**, *38*, 194–205.

77. Doucet, L.S.; Ionov, D.A.; Golovin, A.V. The origin of coarse garnet peridotites in cratonic lithosphere: New data on xenoliths from the Udachnaya kimberlite, central Siberia. *Contrib. Miner. Pet.* **2013**, *165*, 1225–1242. [[CrossRef](#)]
78. Ionov, D.A.; Doucet, L.S.; Strandmann, P.A.E.; Golovin, A.V.; Korsakov, A.V. Links between deformation, chemical enrichments and Li-isotope compositions in the lithospheric mantle of the central Siberian craton. *Chem. Geol.* **2017**, *475*, 105–121. [[CrossRef](#)]
79. Griffin, W.L.; Shee, S.R.; Ryan, C.G.; Win, T.T.; Wyatt, B.A. Harzburgite to lherzolite and back again: Metasomatic processes in ultramafic xenoliths from the wesselton kimberlite, Kimberley, South Africa. *Contrib. Miner. Pet.* **1999**, *134*, 232–250. [[CrossRef](#)]
80. Kostrovitsky, S.I.; Morikiyo, T.; Serov, I.V.; Yakovlev, D.A.; Amirzhanov, A.A. Isotope-geochemical systematics of kimberlites and related rocks from the Siberian platform. *Russ. Geol. Geophys.* **2007**, *48*, 272–290. [[CrossRef](#)]
81. Pokhilenko, N.P.; Sobolev, N.V.; Kuligin, S.S.; Shimizu, N. Peculiarities of distribution of pyroxenite paragenesis garnets in Yakutian kimberlites and some aspects of the evolution of the Siberian craton lithospheric mantle. In Proceedings of the 7th International Kimberlite Conference, Cape Town, South Africa, 17 April 1998; pp. 689–698.
82. Alifirova, T.; Mikhailenko, D.; Korsakov, A.; Golovin, A.; Klemme, S.; Berndt, J. Genetic code of subsolidus garnet and its role in deciphering of Siberian craton metasomatic history. In Proceedings of the EGU General Assembly Conference Abstracts, Vienna, Austria, 8–13 April 2018; p. 841.
83. Gibson, S.A. On the nature and origin of garnet in highly-refractory archaean lithospheric mantle: Constraints from garnet exsolved in Kaapvaal craton orthopyroxenes. *Miner. Mag.* **2017**, *81*, 781–809. [[CrossRef](#)]
84. Ionov, D.A.; Doucet, L.S.; Ashchepkov, I.V. Composition of the lithospheric mantle in the Siberian craton: New constraints from fresh peridotites in the Udachnaya-East kimberlite. *J. Pet.* **2010**, *51*, 2177–2210. [[CrossRef](#)]
85. Stachel, T.; Harris, J.W. The origin of cratonic diamonds—constraints from mineral inclusions. *Ore Geol. Rev.* **2008**, *34*, 5–32. [[CrossRef](#)]
86. Stachel, T.; Harris, J.W. Syngenetic inclusions in diamond from the Birim field (Ghana)—A deep peridotitic profile with a history of depletion and re-enrichment. *Contrib. Miner. Pet.* **1997**, *127*, 336–352. [[CrossRef](#)]
87. Simon, N.S.C.; Irvine, G.J.; Davies, G.R.; Pearson, D.G.; Carlson, R.W. The origin of garnet and clinopyroxene in “depleted” Kaapvaal peridotites. *Lithos* **2003**, *71*, 289–322. [[CrossRef](#)]
88. Boyd, F.R.; Pokhilenko, N.P.; Pearson, D.G.; Mertzman, S.A.; Sobolev, N.V.; Finger, L.W. Composition of the Siberian cratonic mantle: Evidence from Udachnaya peridotite xenoliths. *Contrib. Miner. Pet.* **1997**, *128*, 228–246. [[CrossRef](#)]
89. Gregoire, M.; Bell, D.R.; Roex, A.P.L. Trace element geochemistry of phlogopite-rich mafic mantle xenoliths: Their classification and their relationship to phlogopite-bearing peridotites and kimberlites revisited. *Contrib. Miner. Pet.* **2002**, *142*, 603–625. [[CrossRef](#)]
90. Bryndzia, L.T.; Wood, B.J. Oxygen thermobarometry of abyssal spinel peridotites: The redox state and C–O–H volatile composition of the Earth’s sub-oceanic upper mantle. *Am. J. Sci.* **1990**, *290*, 1093–1116. [[CrossRef](#)]
91. Lee, C.-T.A.; Brandon, A.D.; Norman, M. Vanadium in peridotites as a proxy for paleo-fO₂ during partial melting: Prospects, limitations, and implications. *Geochim. Cosmochim. Acta* **2003**, *67*, 3045–3064. [[CrossRef](#)]
92. Wood, B.J.; Pawley, A.; Frost, D.R.; Jephcoat, A.P.; Angel, R.J.; O’Nions, R.K. Water and carbon in the Earth’s mantle. *Philos. Trans. R. Soc. Lond. Ser. A Math. Phys. Eng. Sci.* **1996**, *354*, 1495–1511. [[CrossRef](#)]
93. Woodland, A.B.; Koch, M. Variation in oxygen fugacity with depth in the upper mantle beneath the Kaapvaal craton, Southern Africa. *Earth Planet. Sci. Lett.* **2003**, *214*, 295–310. [[CrossRef](#)]
94. Litasov, K.D. Physicochemical conditions for melting in the Earth’s mantle containing a C–O–H fluid (from experimental data). *Russ. Geol. Geophys.* **2011**, *52*, 475–492. [[CrossRef](#)]
95. Shirey, S.B.; Cartigny, P.; Frost, D.J.; Keshav, S.; Nestola, F.; Nimis, P.; Pearson, D.G.; Sobolev, N.V.; Walter, M.J. Diamonds and the geology of mantle carbon. *Rev. Miner. Geochem.* **2013**, *75*, 355–421. [[CrossRef](#)]
96. Pokhilenko, N.; Agashev, A.; Litasov, K.; Pokhilenko, L. Carbonatite metasomatism of peridotite lithospheric mantle: Implications for diamond formation and carbonatite-kimberlite magmatism. *Russ. Geol. Geophys.* **2015**, *56*, 280–295. [[CrossRef](#)]
97. Kolganov, V.F.; Akishev, A.N.; Drozdov, A.V. *Mining and Geological Features of the Primary Deposits of Diamonds in Yakutia*; Mirny Printing House: Mirny, Russia, 2013. (In Russian)

98. Malkovets, V.G.; Griffin, W.L.; O'Reilly, S.Y.; Wood, B.J. Diamond, subcalcic garnet, and mantle metasomatism: Kimberlite sampling patterns define the link. *Geology* **2007**, *35*, 339–342. [[CrossRef](#)]
99. Khokhryakov, A.F.; Pal'yanov, Y.N. The evolution of diamond morphology in the process of dissolution: Experimental data. *Am. Miner.* **2007**, *92*, 909–917. [[CrossRef](#)]
100. Khokhryakov, A.F.; Pal'yanov, Y.N. Influence of the fluid composition on diamond dissolution forms in carbonate melts. *Am. Miner.* **2010**, *95*, 1508–1514. [[CrossRef](#)]
101. Fedortchouk, Y.; Manghnani, M.H.; Hushur, A.; Shiryaev, A.; Nestola, F. An atomic force microscopy study of diamond dissolution features: The effect of H₂O and CO₂ in the fluid on diamond morphology. *Am. Miner.* **2011**, *96*, 1768–1775. [[CrossRef](#)]
102. Kozai, Y.; Arima, M. Experimental study on diamond dissolution in kimberlitic and lamproitic melts at 1300–1420 °C and 1 GPa with controlled oxygen partial pressure. *Am. Miner.* **2005**, *90*, 1759–1766. [[CrossRef](#)]
103. Robinson, D.; Scott, J.; Niekerk, A.V.; Anderson, V. Events reflected in the diamonds of some southern African kimberlites. In Proceedings of the Fourth International Kimberlite Conference: Extended Abstracts, Perth, Western Australia, 11–15 August 1986; pp. 421–423.
104. Fedortchouk, Y.; Canil, D.; Carlson, J.A. Dissolution forms in Lac de Gras diamonds and their relationship to the temperature and redox state of kimberlite magma. *Contrib. Miner. Pet.* **2005**, *150*, 54–69. [[CrossRef](#)]
105. Shirey, S.B.; Shigley, J.E. Recent advances in understanding the geology of diamonds. *Gems Gemol.* **2013**, *49*, 188–222. [[CrossRef](#)]
106. Nowicki, A.V.; Galloway, M.; Roex, A.L.; Gurney, J.; Smith, C.; Canil, D. Iron-in-perovskite oxygen barometry and diamond resorption in kimberlites and lamproites from southern Africa, Russia and Australia. In Proceedings of the 9th International Kimberlite Conference, Frankfurt, Germany, 10–15 August 2008; p. abstract No. 9IKC-A-00301.
107. Kharkiv, A.D.; Zinchuk, N.N.; Kryuchkov, A.I. *Primary Diamond Deposits of the World*; Nedra: Moscow, Russia, 1998; p. 555. (In Russian)
108. Zinchuk, N.N.; Koptil, V.I. *Typomorphizm of the Siberian Platmorm Diamonds*; Nedra: Moscow, Russia, 2003; p. 603. (In Russian)
109. Rielli, A.; Tomkins, A.G.; Nebel, O.; Brugger, J.; Etschmann, B.; Paterson, D. Garnet peridotites reveal spatial and temporal changes in the oxidation potential of subduction. *Sci. Rep.* **2018**, *8*, 16411. [[CrossRef](#)] [[PubMed](#)]
110. McCammon, C.A.; Griffin, W.L.; Shee, S.R.; O'Neill, H.S.C. Oxidation during metasomatism in ultramafic xenoliths from the Wesseltion kimberlite, South Africa: Implications for the survival of diamond. *Contrib. Miner. Pet.* **2001**, *141*, 287–296. [[CrossRef](#)]



© 2020 by the authors. Licensee MDPI, Basel, Switzerland. This article is an open access article distributed under the terms and conditions of the Creative Commons Attribution (CC BY) license (<http://creativecommons.org/licenses/by/4.0/>).